



Activating transition metal via synergistic anomalous phase and doping engineering towards enhanced dehydrogenation of ammonia borane

Ping Li ^{a,b,*}, Ran Chen ^{a,b}, Yuqi Huang ^{a,b}, Wenqin Li ^{a,b}, Shien Zhao ^{a,b}, Shuanghong Tian ^{a,b}

^a School of Environmental Science and Engineering, Sun Yat-sen University, Guangzhou 510275, Guangdong, PR China

^b Guangdong Provincial Key Laboratory of Environmental Pollution Control and Remediation Technology, Guangzhou 510275, PR China



ARTICLE INFO

Keywords:

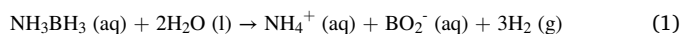
Transition metal nanocatalyst
Crystal phase engineering
Heteroatom doping
Electronic modulation
Ammonia borane dehydrogenation

ABSTRACT

Seeking high-performing non-noble transition metal catalysts for hydrogen evolution from chemical hydrogen storage media is significant. Herein we demonstrate for the first time that anomalous crystal phase engineering coupled with heteroatom doping can remarkably activate transition metal (Ni as a proof-of-concept study) for boosting ammonia borane (AB) dehydrogenation. Ni nanoparticles with designated phase (fcc or hcp phase) encapsulated in carbon (fcc-Ni/C and hcp-Ni/C) can be readily derived from Ni-based MOF. Intriguingly, hcp-Ni/C featuring unconventional hcp phase can remarkably outperform fcc-Ni/C with common fcc phase in AB dehydrogenation. Moreover, by doping Cu, dramatically promoted catalysis can be further achieved for hcp-CuNi/C. From experimental and theoretical results, delicate crystal phase together with heteroatom doping engineering can optimize electronic structure of hcp-CuNi/C, facilitating rate-determining step (H_2O dissociation), thereby boosting AB hydrolysis. This study details the first insight into the phase and doping engineering over non-noble transition metals for promoting AB dehydrogenation.

1. Introduction

Hydrogen (H_2) is regarded as a promising energy carrier to substitute the traditional fossil fuels owing to its high energy density and no-carbon emission [1–3]. Efficient and safe hydrogen storage and release technology is indispensable, yet challenging [4–7]. Ammonia borane (NH_3BH_3 , AB) is considered as an appealing hydrogen storage material because of its high hydrogen content (19.6 wt%, 146 g L^{-1}), good stability under ambient condition, as well as non-toxicity [8]. Facile hydrogen evolution can be achieved via catalytic hydrolysis of AB (Eq. (1)), and the efficiency of this route is highly dependent on the catalyst [8–16].



To date, transition metals are the most widely used catalysts for the hydrolytic dehydrogenation of AB [9,17–19]. Among them, noble metals (such as Pt, Rh, and Ru) are identified as the state-of-the-art catalysts, while their high cost and limited natural abundance seriously restrict their large-scale applications [10,17,20–23]. Consequently, developing high-performance yet economical non-noble transition metals (such as Fe, Co, Ni, and Cu) for AB hydrolysis has

attracted intensive research interest [9,10,17,18,24–27]. In the past decade, to activate and optimize non-noble transition metal catalysts for AB hydrolysis, numerous approaches have been exploited, including the control of chemical composition, size, shape, dimension, and architecture, etc [18,25,28–30]. Notwithstanding the progress already made, non-noble transition metals still display limited catalytic AB dehydrogenation performance, underperforming the well-established noble metals. Therefore, it is highly desirable to develop new strategies to further promote the catalytic properties of the non-noble transition metals for AB hydrolysis, yet remains a huge challenge.

Crystal phase engineering has recently emerged as a powerful protocol to tailor the properties and functions of the nanomaterials [31–33]. In principle, different crystal phases possess varied atom stacking modes, thus lead to distinct crystal structures and surface electronic structures, thereby making a substantial impact on their intrinsic catalytic properties [34–37]. So far, control of crystal phase for boosting performance has been reported to be available in some energy storage/conversion systems [38–42]. However, studies of crystal phase engineering over non-noble transition metals to regulate catalytic AB hydrolysis behavior are lacking, and the correlation between crystal phase and catalytic AB dehydrogenation activity is still unknown, thus

* Corresponding author at: School of Environmental Science and Engineering, Sun Yat-sen University, Guangzhou 510275, Guangdong, PR China.
E-mail address: liping56@mail.sysu.edu.cn (P. Li).

motivating an in-depth investigation.

Based on the above considerations, we herein present for the first time the feasibility of crystal phase engineering over non-noble transition metals for boosted AB dehydrogenation. Nickel (Ni), ranking the fourth most abundant transition metal on the earth [43], is selected as a model catalyst for the proof-of-concept study. Ni can adopt two types of crystal phases, i.e., face-centered cubic (fcc) phase and hexagonal close-packed (hcp) phase [44,45]. The fcc phase of Ni is thermodynamically stable and the most common phase, and almost all the previously reported Ni for AB hydrolysis are focused on the fcc phase [10, 17,25,28,46,47]. By sharp contrast, the utilization of Ni with unconventional hcp phase is rarely reported, as such hcp phase is intrinsically metastable, and the fabrication is limited and challenging.

In this work, carbon-encapsulated Ni nanoparticles (NPs) with designated crystal phase (denoted as fcc-Ni/C and hcp-Ni/C) can be readily constructed via controlled pyrolysis of a Ni-based metal-organic frameworks (MOF) together with hexamethylenetetramine (HMTA) under varied temperatures. Quite intriguingly, the resulting samples exhibit obvious crystal phase-dependent catalytic performance for AB hydrolysis. Particularly, hcp-Ni/C featuring unconventional hcp phase can remarkably outperform the fcc-Ni/C counterpart, unveiling the vital role of phase engineering in catalytic AB hydrolysis. More encouragingly, heteroatomic Cu species doping engineering is found to be able to further considerably boost AB hydrolysis. As a result, with synergistic anomalous phase and doping engineering, the as-obtained product hcp-CuNi/C (turnover frequency (TOF) = 22.64 min⁻¹) can display up to 10 times of activity enhancement relative to the pristine fcc-Ni/C (TOF = 2.10 min⁻¹). From the experimental observations together with density functional theory (DFT) calculations, it is illuminated that both crystal phase engineering and foreign Cu species doping can effectively tailor surface electronic structure of the catalytic centers, lower reaction energy barrier for H₂O dissociation (the rate-determining step), rationalizing the observed boosted AB hydrolysis catalysis.

2. Experimental section

2.1. Preparation of the fcc-Ni/C

Firstly, 6 mmol of Ni(NO₃)₂·6H₂O and 2.25 mL of formic acid (FA) were dissolved in 7.5 mL of *N,N*-dimethylformamide (DMF). The above solution was transferred to a 25 mL of Teflon-lined stainless steel autoclave, sealed and heated at 100 °C for 18 h in an oven. The product was obtained and rinsed with CHCl₃ for several times and dried in a vacuum oven. Then the as-obtained Ni-MOF was put in a tube furnace with hexamethylenetetramine (HMTA) on the upstream side. The tube furnace was heated at 500 °C (heating rate = 2 °C/min) for 2 h with N₂ flowing to convert to the target pyrolysis product, fcc-Ni/C.

2.2. Preparation of the hcp-Ni/C

The hcp-Ni/C was obtained through the similar route for the fcc-Ni/C while using the pyrolysis temperature of 400 °C.

2.3. Preparation of the hcp-CuNi/C

The hcp-CuNi/C was prepared via the similar route for the hcp-Ni/C while adding extra 0.3 mmol of Cu(NO₃)₂·6H₂O during the MOF precursor synthesis.

2.4. Preparation of the hcp-MnNi/C, hcp-FeNi/C, and hcp-CoNi/C

The hcp-MnNi/C, hcp-FeNi/C, and hcp-CoNi/C were prepared via the similar route for the hcp-CuNi/C while using 0.3 mmol of Mn (NO₃)₂·4H₂O, Fe(NO₃)₃·9H₂O, and Co(NO₃)₂·6H₂O to substitute Cu (NO₃)₂·6H₂O in the starting solution, respectively.

2.5. Catalytic performance test

Typically, 10 mg of the catalyst powder was firstly dispersed in 3 mL of 1 M NaOH aqueous solution in a 25 mL of three-necked round bottom flask, and then 1 mmol of AB dissolved in 1 M NaOH aqueous solution (1 mL) was injected from one neck of the flask. The volume of H₂ gas was measured by a typical water displacement system at 298 K. The schematic diagram of the setup can be found in Fig. S1. For conducting the stability test, the catalyst was magnetically recovered and reused for the next cycle under the same condition at 298 K. The TOF value was obtained according to Eq. (2). Herein it is assumed that all the metal species in the samples are catalytically active for AB dehydrogenation, so the calculated TOF values in this study should be considered as the lower limit, since it is understandable that not all the metal species in the catalyst can be fully exposed for catalysis in a real-world scenario. In addition, the hydrolysis of AB was also performed at 303, 308, and 313 K with a temperature-controlled water bath to investigate the reaction activation energy (Ea) according to Eq. (3).

$$\text{TOF} = \frac{m(\text{H}_2\text{O}) / (\rho(\text{H}_2\text{O}) * 24.5)}{n(\text{cat} - \text{TM}) * t(\text{min})} \quad (2)$$

$$\text{ln}k = \text{ln}A - \text{Ea}/RT \quad (3)$$

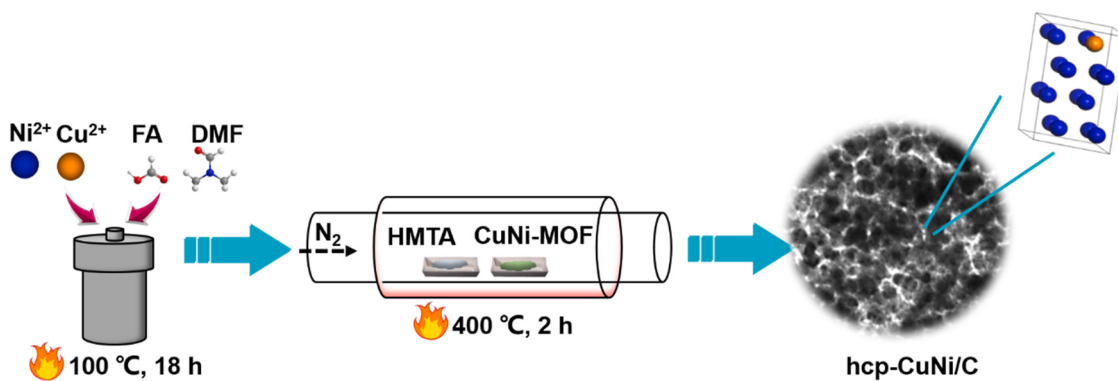
where k is the reaction rate, A is the pre-exponential factor, R is the gas constant, and T is the temperature.

3. Results and discussion

3.1. Preparation and characterization of the samples

The fcc-Ni/C and hcp-Ni/C were fabricated through facile controlled pyrolysis of a Ni-containing MOF (see details in Section 2), and the synthetic route is described in Scheme S1. Firstly, Ni-MOF in hexagonal nanoplate morphology was obtained via a simple solvothermal method with Ni(NO₃)₂·6H₂O as the metal source and FA as the organic ligand (the detailed characterizations of the Ni-MOF are listed in Figs. S2 and S4). Then the Ni-MOF was subjected to a pyrolysis treatment with HMTA under inert gas atmosphere, producing hcp-Ni/C and fcc-Ni/C at 400 °C and 500 °C, respectively. Additionally, the doping-engineered sample hcp-CuNi/C was prepared using the same method as hcp-Ni/C while adding a certain amount of Cu(NO₃)₂·6H₂O together with Ni (NO₃)₂·6H₂O during the solvothermal treatment to yield CuNi-MOF as the precursor (Scheme 1, and the detailed characterizations of the CuNi-MOF possessing hexagonal nanoplate morphology are shown in Figs. S3 and S4).

The X-ray diffraction (XRD) analysis was firstly applied to investigate the crystallographic structure of the samples. From the XRD pattern of the fcc-Ni/C (Fig. 1a), all the diffraction peaks can be well assigned to the fcc phase of Ni (PDF card no. 04-0850, the corresponding crystal structure is displayed in Fig. 1b); and in the case of hcp-Ni/C, all the identified peaks can be indexed to the hcp phase of Ni (PDF card no. 45-1027, the corresponding crystal structure is displayed in Fig. 1b). The above analysis reveals that Ni/C with distinct crystal phases (i.e., fcc and hcp) can be conveniently harvested just through pyrolyzing the Ni-MOF together with HMTA at different temperatures. For the metallic Ni, hcp phase is metastable, while fcc phase is thermodynamically stable. Therefore, pyrolyzing the Ni-MOF at relatively lower temperature (400 °C), pure metastable hcp phase Ni can be obtained. When the temperature increases, the metastable hcp phase Ni would convert to the thermodynamically stable fcc phase Ni. After Cu species incorporation, the as-obtained hcp-CuNi/C maintains the original hcp phase, and the peaks assigned to the Cu-based compounds are not detected in the XRD pattern, suggesting that Cu species is homogeneously doped in the hcp-Ni NPs without any phase separation. Notably, it can be observed that the diffraction peaks of hcp-CuNi/C shift towards the lower 2θ angle



Scheme 1. The preparation procedure of the hcp-CuNi/C sample.

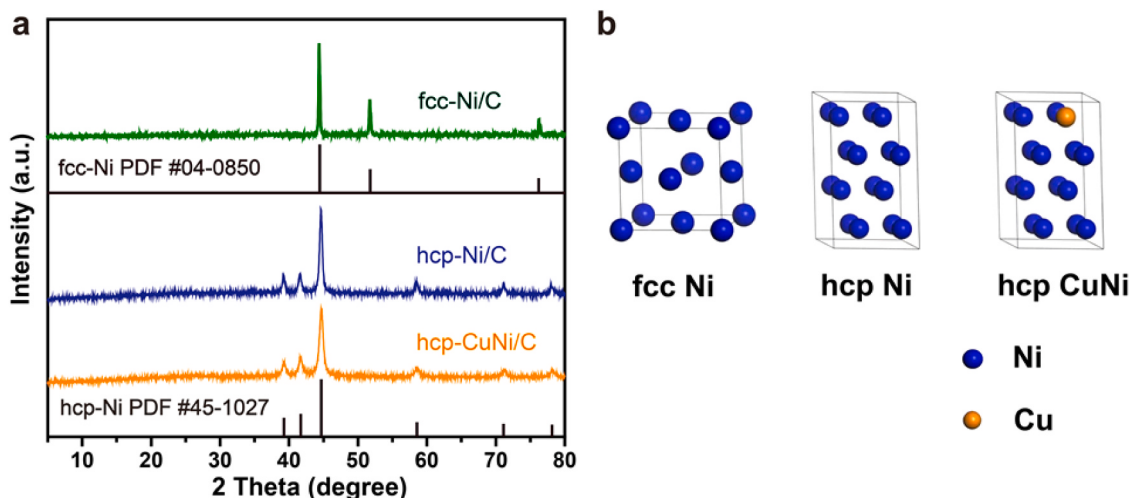


Fig. 1. (a) XRD patterns of the fcc-Ni/C, hcp-Ni/C and hcp-CuNi/C samples. (b) The crystal structures of the fcc-Ni, hcp-Ni and hcp-CuNi.

relative to those of hcp-Ni/C. The above variation can be ascribed to the partial substitution of Ni (atom radius = 1.25 Å) with Cu (atom radius = 1.28 Å) in the sample.

The morphological features of the samples were then studied with SEM and TEM techniques. As displayed the low-magnified SEM images in Fig. 2a and d, both fcc-Ni/C and hcp-Ni/C largely preserve the original hexagonal plate morphology while with porous and rougher surface. Zoom-in TEM images demonstrate that the hexagonal plates in these two samples are composed of numerous interconnected Ni NPs with 10–20 nm in particle size (Fig. 2b and e). Meanwhile, it can be clearly observed that all the Ni NPs are well protected by a thin layer of carbon shells (Fig. 2c and f). In the case of hcp-CuNi/C sample, it presents hexagonal plate morphology consisting of interconnected CuNi NPs encapsulated in thin-layer carbon matrix, resembling the microscopic morphologies of fcc-Ni/C and hcp-Ni/C (Fig. 2g–j). And yet the particle size of CuNi NPs in hcp-CuNi/C are in the range of 30–40 nm (Fig. 2h and i), which is larger than Ni NPs in fcc-Ni/C and hcp-Ni/C (10–20 nm), probably due to foreign Cu species incorporation. The HRTEM image of hcp-CuNi/C in Fig. 2k displays well-resolved lattice fringes with interplanar spacing of 0.187 nm indexed to the (0002) planes of the hcp phase of CuNi. In addition, the EDX elemental mappings (Fig. 2l) display that Ni, Cu, and C elements are homogeneously distributed, further indicating that the Cu element is uniformly doped into the Ni NPs embedded in carbon substrate. From the inductively coupled plasma-optical emission spectrometer (ICP-OES) analysis, the molar ratio of Cu/Ni in hcp-CuNi/C is determined to be about 1:21 (Table S1). Moreover, to evaluate the physical textural properties of the above three samples, N₂ adsorption-desorption measurement was

performed (Fig. S5). The BET specific surface area and total pore volume are 114.0 m²/g and 0.28 cm³/g for fcc-Ni/C, 91.0 m²/g and 0.18 cm³/g for hcp-Ni/C, 58.0 m²/g and 0.12 cm³/g for hcp-CuNi/C.

3.2. Catalytic AB dehydrogenation performance of the samples

The activities of the samples for catalytic dehydrogenation of AB were evaluated at 298 K. The preliminary experiment demonstrated that no H₂ could evolve from AB aqueous solution in the absence of the catalyst, suggesting good stability of AB. As exhibited in Fig. 3a, the precursor materials Ni-MOF and CuNi-MOF show negligible catalytic response. After pyrolysis treatment, fcc-Ni/C with conventional fcc phase becomes active, while displays an impoverished activity, demanding 18 min to complete AB hydrolysis with a TOF value of 2.10 min⁻¹. By marked contrast, hcp-Ni/C with anomalous hcp phase presents significantly enhanced activity, requiring 5 min to finish the reaction with a TOF value of 4.32 min⁻¹. Considering the similar morphological and structural characteristics of fcc-Ni/C and hcp-Ni/C, their distinct catalytic behaviors imply a pronounced effect of the crystal structure on the catalytic activity, and the hcp phase of Ni is more favorable for catalytic AB hydrolysis in comparison with the fcc phase of Ni.

More impressively, it is found that the introduction of Cu species in hcp-Ni/C can further substantially boost AB hydrolysis. Specifically, complete AB dehydrogenation can be achieved within 1.5 min by applying the hcp-CuNi/C as the catalyst, and the TOF value is calculated to be 22.64 min⁻¹, which is obviously much higher than that of undoped counterpart hcp-Ni/C (4.32 min⁻¹). Concerning the origin of the

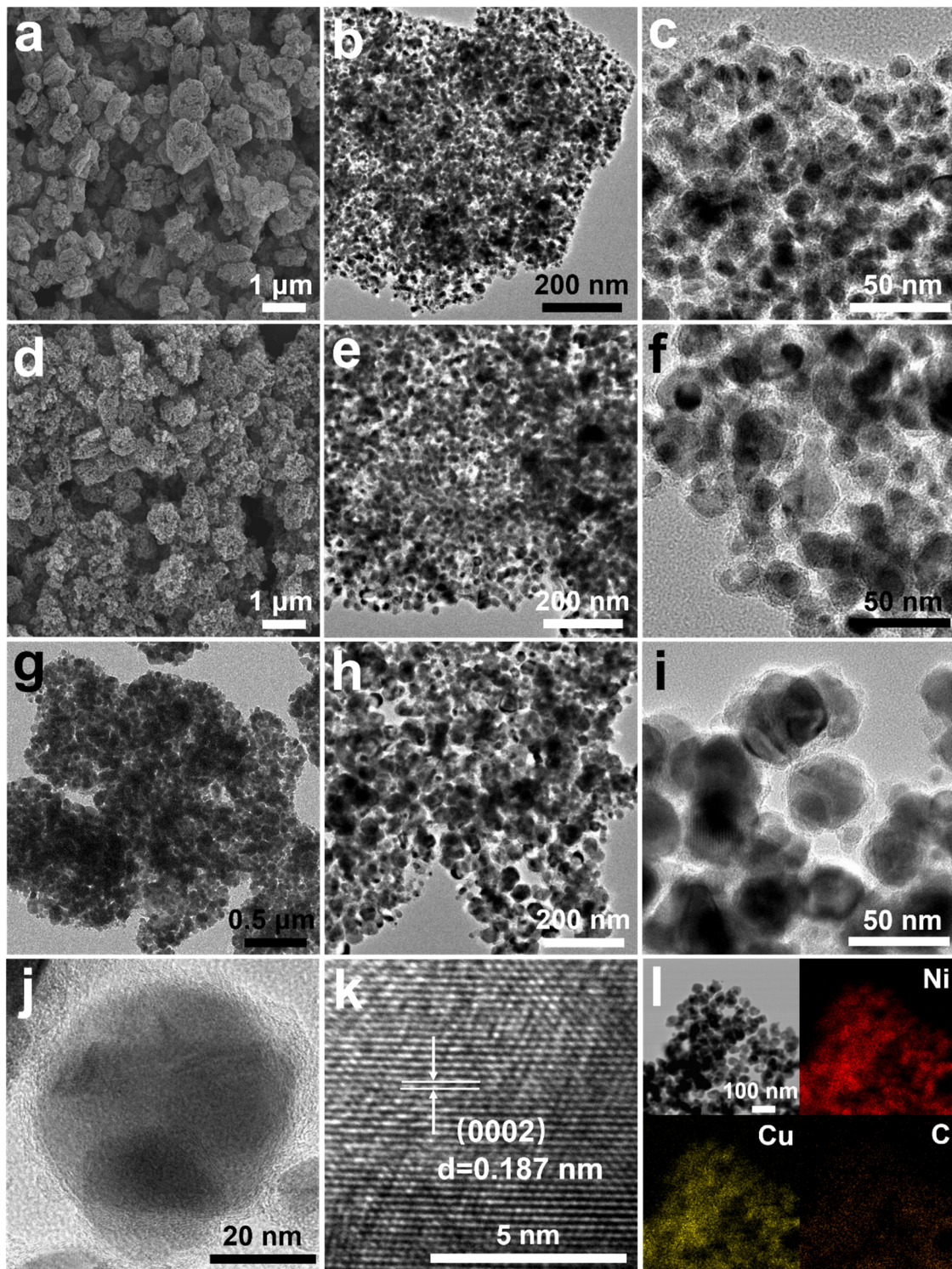


Fig. 2. (a) SEM and (b,c) TEM images of the fcc-Ni/C. (d) SEM and (e,f) TEM images of the hcp-Ni/C. (g–j) TEM images, (k) HRTEM image and (l) EDX elemental mappings of the hcp-CuNi/C sample.

promoted catalytic property of hcp-CuNi/C shown above, it can be ascribed to the presence of a positive synergistic effect between the doping Cu species and the host Ni, which will be detailed in the later part. The above result manifests that the effectiveness of heteroatom doping engineering on optimizing transition metal catalyst for enhanced AB dehydrogenation.

Besides, the reaction kinetics of AB hydrolysis over the fcc-Ni/C, hcp-Ni/C, and hcp-CuNi/C samples were further studied via adjusting the

concentration of AB added. As indicated, in the case of each sample, the volume of hydrogen evolution increases with elevating the concentration of AB, showing a similar hydrogen generation rate (Fig. S6a–c). The slopes of $\ln k$ versus $\ln [AB]$ are determined to be 0.40, 0.28, and 0.32 for fcc-Ni/C, hcp-Ni/C, and hcp-CuNi/C, respectively, signifying AB hydrolysis catalyzed by these three samples are quasi-zero-order with respect to the AB concentration (Fig. S6d). The above result suggests that AB is easy to activate, and the activation of AB is not the rate-

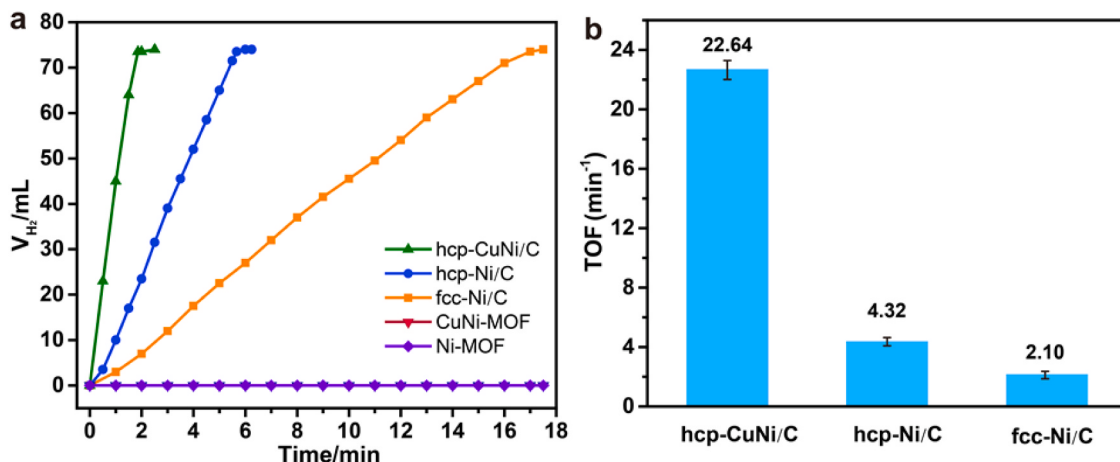


Fig. 3. (a) Hydrogen evolution from AB dehydrogenation in 1 M NaOH solution at 298 K over different catalysts: Ni-MOF, CuNi-MOF, fcc-Ni/C, hcp-Ni/C, and hcp-CuNi/C samples. (b) The corresponding TOF values.

determining step (RDS) under the present conditions.

Additionally, to evaluate the E_a over fcc-Ni/C, hcp-Ni/C and hcp-CuNi/C samples, AB hydrolysis was also tested at different temperatures ranging from 298 K to 313 K with 5 K increment. As displayed in Fig. 4a–c, the rate of hydrogen evolution increases obviously with the increase of the temperature. According to the Arrhenius plot ($\ln k = \ln k_0 - E_a/RT$), the E_a for the dehydrogenation of AB over fcc-Ni/C, hcp-Ni/C and hcp-CuNi/C are calculated to be 40.15, 35.49 and 29.92 kJ mol^{-1} ,

respectively (Fig. 4d). Encouragingly, it is worth noting that the hcp-CuNi/C presented in this work, with a TOF value of 22.64 min^{-1} and an E_a of $29.92 \text{ kJ mol}^{-1}$, can favorably compete with the state-of-the-art catalysts reported to date [30,48–50]. A detailed comparison between hcp-CuNi/C and the previously reported catalysts for the hydrolysis of AB is summarized in Table S2. Based on the above analysis, it is obviously demonstrated that crystal phase engineering coupled with heteroatom doping is a powerful approach to dramatically activate the

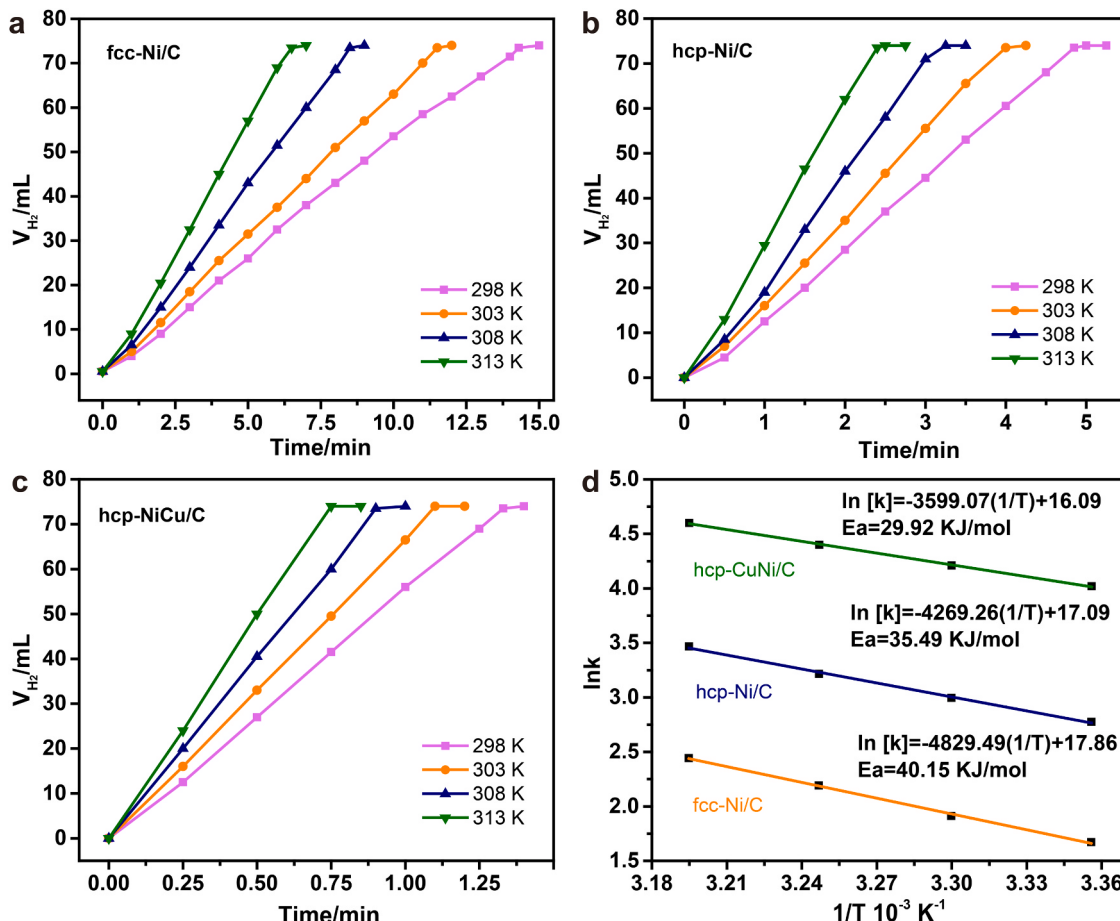


Fig. 4. Volume of hydrogen evolution from AB dehydrogenation versus time at different temperatures (298–313 K) in 1 M NaOH solution catalyzed by different catalysts: (a) fcc-Ni/C, (b) hcp-Ni/C and (c) hcp-CuNi/C. (d) The corresponding Arrhenius plots.

non-noble transition metal for boosted AB dehydrogenation catalysis.

Stability of the catalyst is another crucial parameter for its practical application. The continuous recycling test of the AB hydrolysis over the hcp-CuNi/C sample was performed at 298 K. As shown in Fig. 5a, the catalyst can be reused for up to 8 cycles without significant decline of the activity, suggesting respectable recyclability of the hcp-CuNi/C. Furthermore, the XRD, SEM and TEM images (Fig. 5b-d) reveal that the original morphology and structure of the spent catalyst are largely retained, further implying the robustness of the hcp-CuNi/C. With outstanding catalytic activity and recommendable stability, our cost-effective and readily available hcp-CuNi/C performs as a class of advanced catalyst system for hydrogen evolution from AB dehydrogenation.

3.3. Versatility of the synergistic modulation strategy

To explore the versatility of our protocol to regulate the catalytic AB dehydrogenation behavior through crystal phase engineering together with heteroatom doping, we have constructed a series of transition metal (i.e., Mn, Fe, and Co)-engineered Ni NPs with unconventional hcp phase, including hcp-MnNi/C, hcp-FeNi/C, and hcp-CoNi/C. The preparation procedures can be found in Experimental section, and the metal compositions of the samples based on the ICP-OES analysis were listed in Table S1. From their SEM images (Fig. 6a-c), it can be observed that all these samples possess similar hexagonal plate morphology composed of numerous interconnected NPs, resembling that of hcp-CuNi/C. Further, as exhibited their XRD patterns in Fig. 6d, all the peaks can be well ascribed to the hcp phase of Ni (PDF card no. 45-1027), suggesting that foreign transition metal species is incorporated in the hcp-Ni without

phase separation. Then their catalytic activities for AB hydrolysis were studied. As displayed in Fig. 6e, hcp-MnNi/C, hcp-FeNi/C, and hcp-CoNi/C can exhibit promoted catalysis relative to both fcc-Ni/C and hcp-Ni/C, requiring 5.0, 4.5, and 3.5 min for full reaction, respectively, demonstrating the universality of our strategy. Of note, herein the series of transition metal-engineered bimetallic samples could display different catalytic activities for AB hydrolysis. The above phenomenon can be interpreted from the fact that incorporating different heteroatom species (Mn, Fe, and Co in this study) with varied atomic properties would give rise to distinct surface electronic structure of the Ni host, thereby influencing adsorption/desorption behaviors of the reaction intermediate species, consequently delivering varied catalytic activities. Once again, it suggests the vital impact of the crystal phase engineer and heteroatom doping on tailoring the catalytic property of the catalyst.

3.4. Study of the origin of enhanced catalytic performance

As demonstrated, for the samples studied in this work, their catalytic activities for AB dehydrogenation are in the order of hcp-CuNi/C > hcp-Ni/C > fcc-Ni/C. Based on the systematical characterizations (i.e., SEM, TEM, XRD, and N₂ adsorption-desorption measurement), both fcc-Ni/C and hcp-Ni/C possess similar morphology, dimension, particle size, and surface area, thus their variation in catalytic properties can be interpreted from the crystal phase effect. With distinct stacking modes of atoms, it is understandable that the hcp-Ni and fcc-Ni possess different crystal structures and surface electronic structures, thus giving rise to deliver different catalytic behaviors. On the other hand, compared with hcp-Ni/C, hcp-CuNi/C displays similar morphology while with larger metal particle size (30–40 nm vs. 10–20 nm of hcp-Ni/C) and lower BET

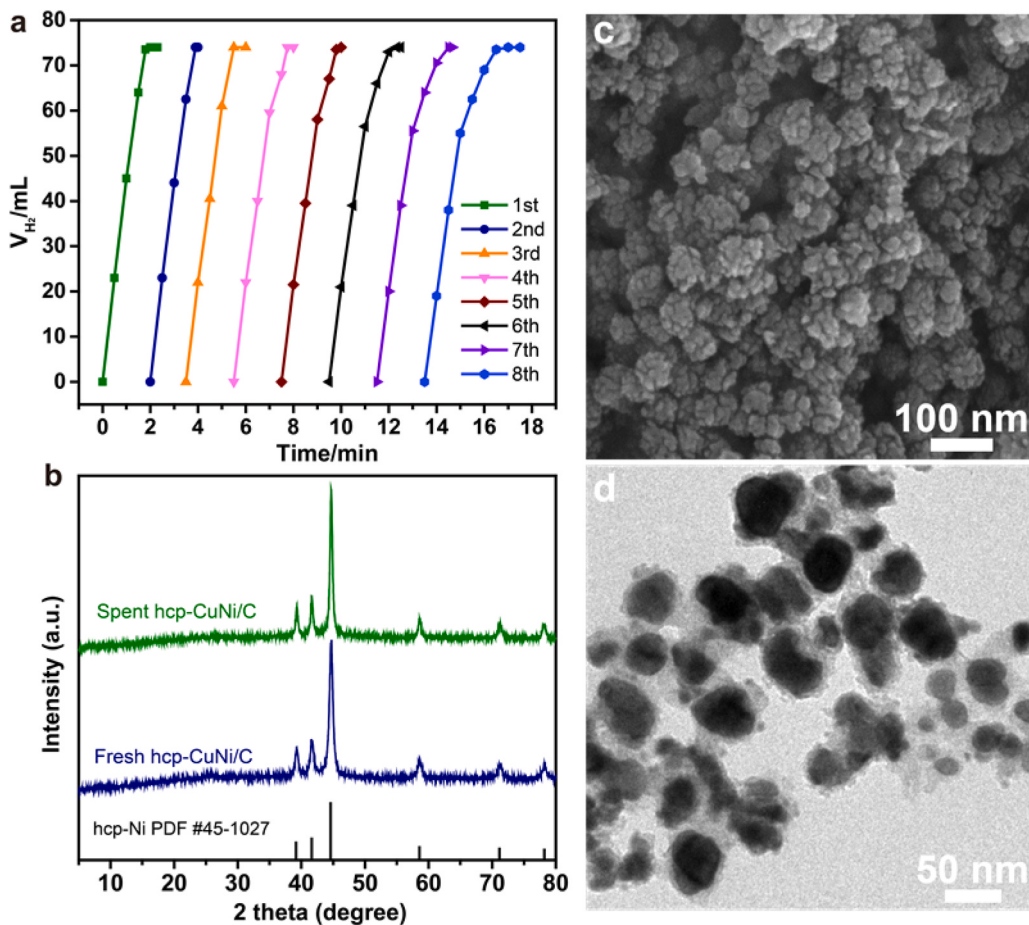


Fig. 5. (a) The cycling test of the AB hydrolytic dehydrogenation over the hcp-CuNi/C sample. The characterizations of the spent hcp-CuNi/C after the cycling test: (b) XRD pattern, (c) SEM image, and (d) TEM image.

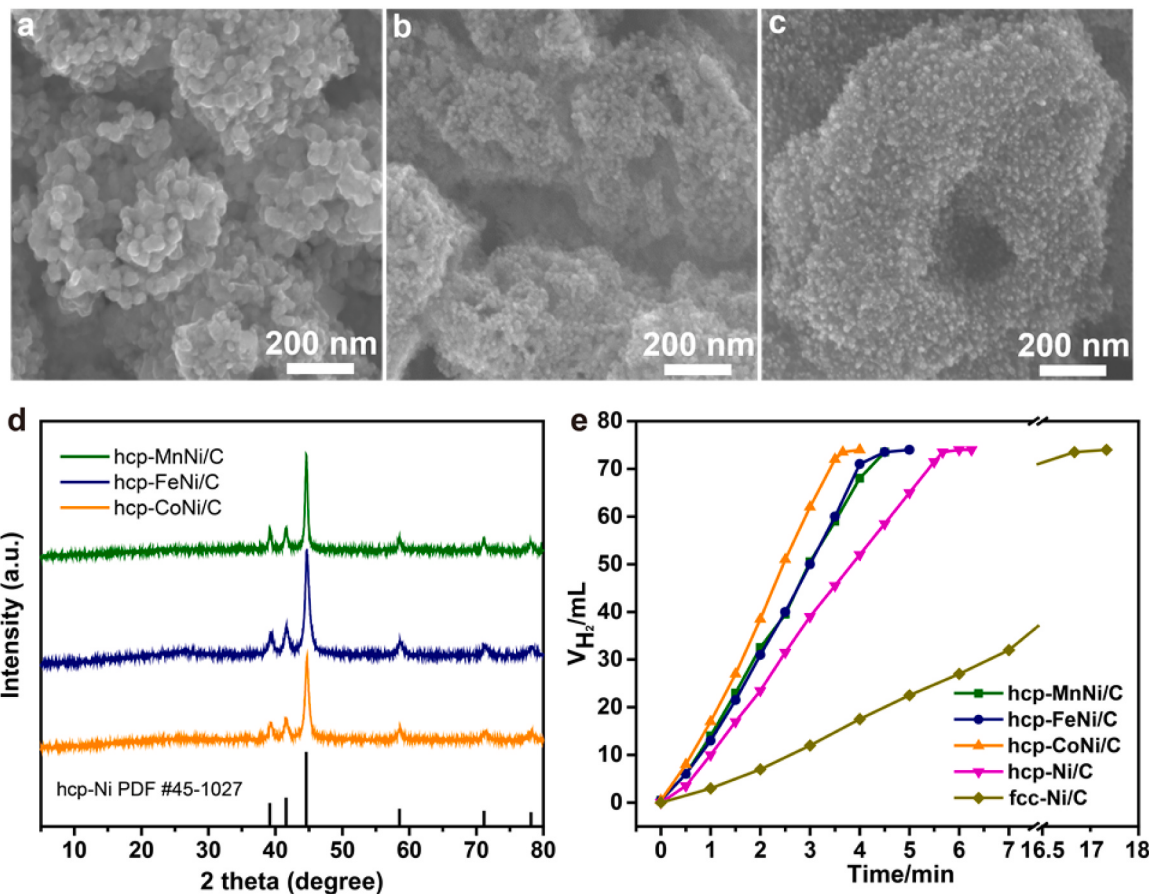


Fig. 6. SEM images of (a) hcp-MnNi/C, (b) hcp-FeNi/C, and (c) hcp-CoNi/C samples. (d) XRD patterns of the three samples. (e) Hydrogen evolution from AB dehydrogenation at 298 K catalyzed by different samples.

surface area ($58.0 \text{ m}^2/\text{g}$ vs. $91.0 \text{ m}^2/\text{g}$ of hcp-Ni/C). Nevertheless, hcp-CuNi/C can still strikingly outperform hcp-Ni/C for catalyzing AB hydrolysis, revealing much higher intrinsic activity of hcp-CuNi/C with Cu species engineering. It is reasonable to infer that foreign Cu species doping in hcp-CuNi/C can elegantly modulate the coordination environment and electronic configuration of Ni sites, yielding optimized surface electronic structure for the targeted catalytic reaction.

To elucidate the point better, XPS analysis was firstly performed on the hcp-CuNi/C and hcp-Ni/C to study the electronic interaction. Fig. 7a

shows the Cu 2p spectrum of hcp-CuNi/C, the peaks at 932.8 and 934.7 eV can be assigned to the metallic Cu and oxidized Cu species (from superficial oxidation during sample storage and handling), respectively [51,52], substantiating that Cu species successfully incorporates in hcp-CuNi/C. In the Ni 2p spectra (Fig. 7b), hcp-CuNi/C shows the peaks at 852.9 and 856.0 eV which can be corresponded to the metallic Ni and oxidized Ni species, respectively [25,53–55]. Notably, relative to the hcp-Ni/C, Ni 2p peaks in the hcp-CuNi/C are shifted to higher binding energies, indicating decreased electron density

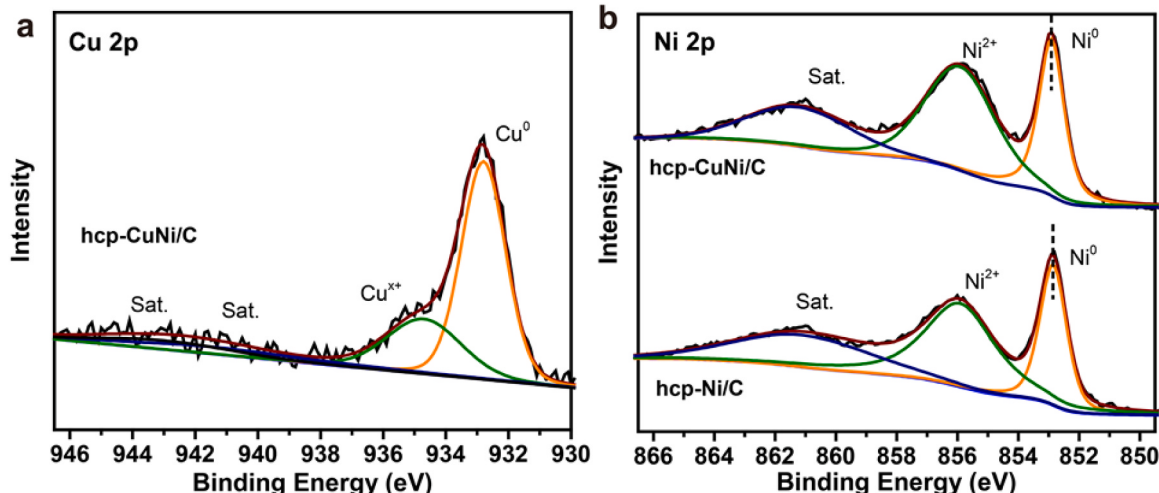


Fig. 7. The XPS spectra of the hcp-CuNi/C and hcp-Ni/C samples: (a) Cu 2p and (b) Ni 2p.

of Ni species once Cu incorporation. That is to say, foreign Cu doping can efficiently tailor the electronic configuration of the hcp-CuNi/C.

Additionally, it has been widely acknowledged that the initial water adsorption is vital to launch the catalytic AB hydrolysis [26,56]. Thus, the water contact angle measurement was carried out over the fcc-Ni/C, hcp-Ni/C and hcp-CuNi/C samples to study their wettability properties. As clearly shown in Fig. S7a–c, the three samples are hydrophilic, and the hcp-Ni/C and hcp-CuNi/C exhibit initial contact angles of 35.4° and 36.5°, respectively, smaller than that of fcc-Ni/C (43.2°), demonstrating that crystal phase engineering is a feasible way to regulate the wettability of the catalyst, and the hcp phase Ni is more hydrophilic than the fcc counterpart. Apparently, the improved hydrophilicity of hcp-CuNi/C could be expected to benefit the smooth diffusion of H_2O and AB, rendering promoted AB hydrolysis process.

To unveil more insight into the pronounced effect of crystal phase and doping engineering on the catalytic dehydrogenation of AB, DFT calculations were carried out. Herein the fcc-Ni(111), hcp-Ni(0001), and hcp-CuNi(0001) were modeled to represent the catalyst surfaces. The density of states (DOS) of the fcc-Ni(111), hcp-Ni(0001), and hcp-CuNi

(0001) are illustrated in Fig. 8a–c. As clearly demonstrated, with crystal phase engineering or/and Cu doping, variations of the DOS can be achieved for hcp-Ni(0001) and hcp-CuNi(0001), signifying the modification of electronic property.

Further, according to the previous contributions, H_2O adsorption on the catalyst is prerequisite to start the reaction, and H_2O dissociation to generate the adsorbed OH^* and H^* species on the catalyst surface is the rate-determining step which dominates the overall rate of AB hydrolysis [20,21,25,26,57]. As shown in Fig. 8d, all the three model surfaces, fcc-Ni(111), hcp-Ni(0001), and hcp-CuNi(0001) are ready for H_2O adsorption with a similar H_2O binding energy ($E_{\text{b}(\text{H}_2\text{O})}$) of -0.303 eV, -0.305 eV, and -0.298 eV, respectively. On the other hand, the reaction energy barrier for H_2O dissociation ($E_{\text{ac}(\text{H}_2\text{O})}$) on the catalysts were analyzed. Fig. 8e displays the atomic structures of key reaction states of the hcp-CuNi(0001) for H_2O dissociation, and the energy profiles of the H_2O dissociation over the samples are summarized in Fig. 8f. It is found that hcp-CuNi(0001) possesses the lowest $E_{\text{ac}(\text{H}_2\text{O})}$ with a value of 0.89 eV, followed by hcp-Ni(0001) (0.93 eV) and fcc-Ni(111) (1.01 eV), revealing that unconventional hcp phase design and Cu

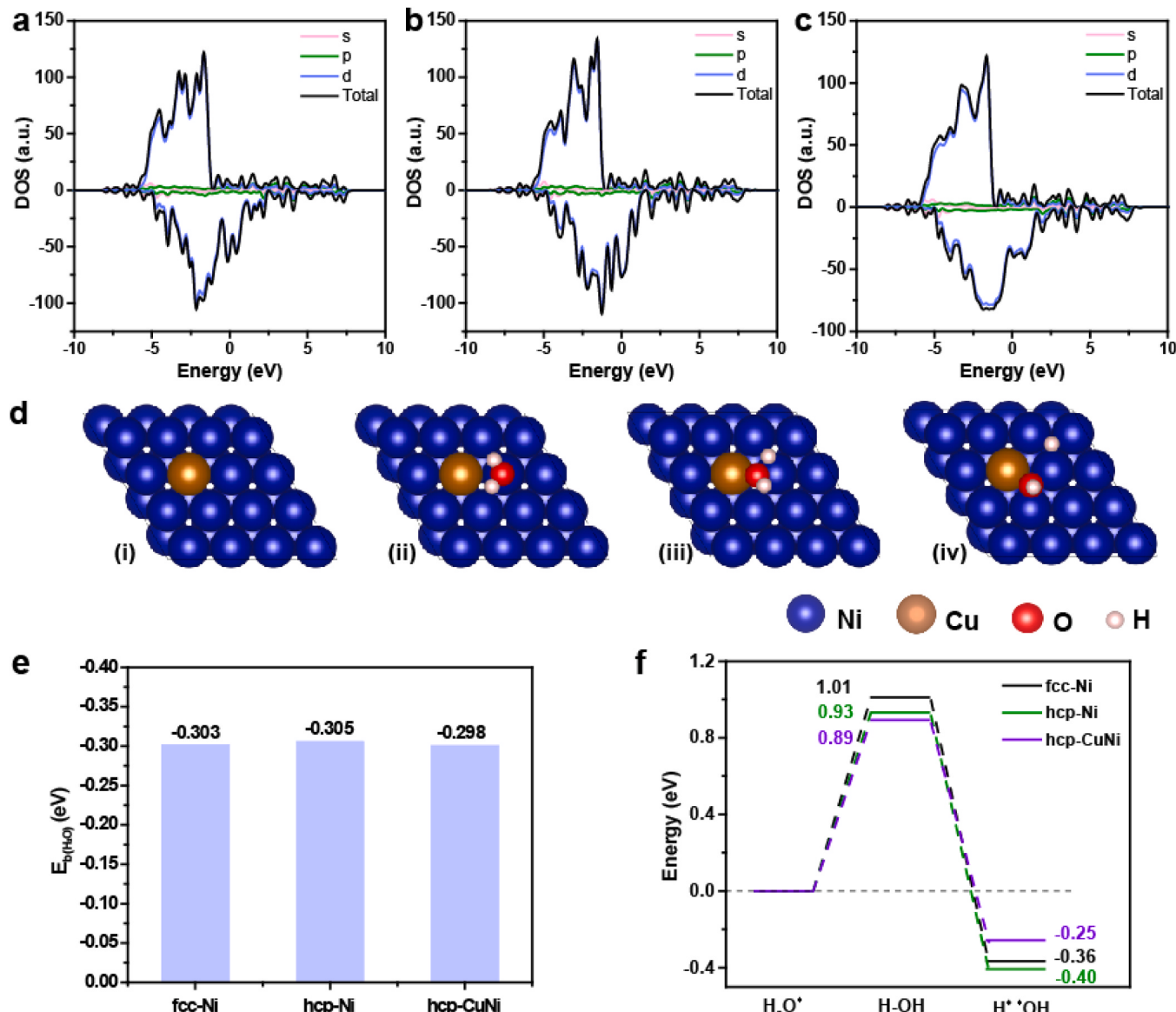


Fig. 8. The density of states (DOS) of the (a) fcc-Ni(111), (b) hcp-Ni(0001), and (c) hcp-CuNi(0001) model surfaces. (d) The atomic structures of key reaction states of the hcp-CuNi(0001) for H_2O dissociation: (i) clean surface, (ii) initial state, (iii) transition state, (iv) final state. (e) The H_2O binding energy ($E_{\text{b}(\text{H}_2\text{O})}$) and (f) the energy profiles of H_2O dissociation over different model surfaces.

species incorporation over the metallic Ni can effectively boost H_2O cleavage. Taken together, according to the DFT calculations, the superior catalytic activity of hcp-CuNi/C for AB hydrolytic dehydrogenation originates from the optimized electronic configuration endowed by the crystal phase engineering together with Cu doping, efficiently promoting the rate-determining step of H_2O dissociation.

4. Conclusion

In summary, we report for the first time that anomalous crystal phase engineering together with heteroatom doping is an efficient approach to activate the non-noble transition metal for promoted AB hydrolytic dehydrogenation. Take Ni-based catalyst as an example, it is impressively disclosed that hcp-Ni/C featuring unconventional hcp phase is able to present much better catalytic efficiency for AB dehydrogenation with respect to the fcc-Ni/C counterpart in common fcc phase. More encouragingly, incorporation of Cu species in hcp-CuNi/C can further significantly boost the catalytic reaction. As confirmed from the experimental studies and DFT calculations, simultaneously engineering over crystal phase and foreign Cu species doping can regulate the surface electronic state of the hcp-CuNi/C to lower the reaction energy barrier for H_2O dissociation (the rate-determining step), and thus dramatically accelerating AB hydrolytic dehydrogenation. This work is expected to provide a fresh insight for activating the non-noble transition metal catalyst through synergistic modulation of crystal phase and heteroatom doping to substantially expedite AB dehydrogenation, and meanwhile, give inspirations on developing other advanced material systems for catalysis.

CRediT authorship contribution statement

Ping Li: Conceptualization, Project administration, Writing – review & editing, Supervision, Funding acquisition. **Ran Chen:** Conceptualization, Methodology, Formal analysis, Investigation, Resources, Visualization, Writing – original draft. **Yuqi Huang:** Resources, Methodology, Investigation, Data curation, Validation. **Wenqin Li:** Data curation, Validation. **Shien Zhao:** Resources, Validation. **Shuanghong Tian:** Supervision, Writing – review & editing.

Declaration of Competing Interest

The authors declare that they have no known competing financial interests or personal relationships that could have appeared to influence the work reported in this paper.

Acknowledgements

The research is supported by the National Natural Science Foundation of China (No. 52002412 and 22072186), the Natural Science Foundation of Guangdong Province (2021A1515010575), Guangzhou Science and Technology Plan General Project (202102020862), the Start-up Funds for High-Level Talents of Sun Yat-sen University (38000-18841206), and the Fundamental Research Funds for the Central Universities (19lgpy156).

Supplementary data

Additional SEM images, FTIR spectra, XRD patterns, N_2 adsorption-desorption measurement results, dynamic water contact angle measurement results, ICP-OES analysis, and catalytic performance result of the samples. Supplementary data associated with this article can be found in the online version, at <http://XXX>.

Appendix A. Supporting information

Supplementary data associated with this article can be found in the

online version at [doi:10.1016/j.apcatb.2021.120725](https://doi.org/10.1016/j.apcatb.2021.120725).

References

- [1] T. He, P. Pachfule, H. Wu, Q. Xu, P. Chen, Hydrogen carriers, *Nat. Rev. Mater.* 1 (2016) 16059.
- [2] S. Dunn, Hydrogen futures: toward a sustainable energy system, *Int. J. Hydrog. Energy* 27 (2002) 235–264.
- [3] M.K. Singla, P. Nijhawan, A.S. Oberoi, Hydrogen fuel and fuel cell technology for cleaner future: a review, *Environ. Sci. Pollut. Res. Int.* 28 (2021) 15607–15626.
- [4] L. Schlapbach, A. Züttel, Hydrogen-storage materials for mobile applications, *Nature* 414 (2001) 353–358.
- [5] C. Lang, Y. Jia, X. Yao, Recent advances in liquid-phase chemical hydrogen storage, *Energy Storage Mater.* 26 (2020) 290–312.
- [6] M. Yue, H. Lambert, E. Pahon, R. Roche, S. Jemei, D. Hissel, Hydrogen energy systems: a critical review of technologies, applications, trends and challenges, *Renew. Sustain. Energy Rev.* 146 (2021), 111180.
- [7] J. Yang, A. Sudik, C. Wolverton, D.J. Siegel, High capacity hydrogen storage materials: attributes for automotive applications and techniques for materials discovery, *Chem. Soc. Rev.* 39 (2010) 656–675.
- [8] A. Staubitz, A.P.M. Robertson, I. Manners, Ammonia-borane and related compounds as dihydrogen sources, *Chem. Rev.* 110 (2010) 4079–4124.
- [9] C. Yüksel Alpaydin, S.K. Gülbay, C. Ozgur Colpan, A review on the catalysts used for hydrogen production from ammonia borane, *Int. J. Hydrog. Energy* 45 (2020) 3414–3434.
- [10] C. Wang, Q. Wang, F. Fu, D. Astruc, Hydrogen generation upon nanocatalyzed hydrolysis of hydrogen-rich boron derivatives: recent developments, *Acc. Chem. Res.* 53 (2020) 2483–2493.
- [11] X. Du, C. Yang, X. Zeng, T. Wu, Y. Zhou, P. Cai, G. Cheng, W. Luo, Amorphous NiP supported on rGO for superior hydrogen generation from hydrolysis of ammonia borane, *Int. J. Hydrog. Energy* 42 (2017) 14181–14187.
- [12] C.-C. Hou, Q. Li, C.-J. Wang, C.-Y. Peng, Q.-Q. Chen, H.-F. Ye, W.-F. Fu, C.-M. Che, N. López, Y. Chen, Ternary Ni–Co–P nanoparticles as noble-metal-free catalysts to boost the hydrolytic dehydrogenation of ammonia-borane, *Energy Environ. Sci.* 10 (2017) 1770–1776.
- [13] D. Lu, J. Li, C. Lin, J. Liao, Y. Feng, Z. Ding, Z. Li, Q. Liu, H. Li, A simple and scalable route to synthesize $\text{Co}_x\text{Cu}_1-x\text{Co}_2\text{O}_4@\text{Co}_x\text{Cu}_1-y\text{Co}_2\text{O}_4$ yolk-shell microspheres, a high-performance catalyst to hydrolyze ammonia borane for hydrogen production, *Small* 15 (2019), 1805460.
- [14] H. Song, Y. Cheng, B. Li, Y. Fan, B. Liu, Z. Tang, S. Lu, Carbon dots and Ru₂ nanohybrid as an efficient bifunctional catalyst for electrochemical hydrogen evolution reaction and hydrolysis of ammonia borane, *ACS Sustain. Chem. Eng.* 8 (2020) 3995–4002.
- [15] H. Sun, J. Meng, L. Jiao, F. Cheng, J. Chen, A review of transition-metal boride/phosphide-based materials for catalytic hydrogen generation from hydrolysis of boron-hydrides, *Inorg. Chem. Front.* 5 (2018) 760–772.
- [16] P. Li, R. Chen, S. Zhao, W. Li, Y. Lin, Y. Yu, Architecture control and electronic structure engineering over Ni-based nitride nanocomposite for boosting ammonia borane dehydrogenation, *Appl. Catal. B Environ.* 298 (2021), 120523.
- [17] W.-W. Zhan, Q.-L. Zhu, Q. Xu, Dehydrogenation of ammonia borane by metal nanoparticle catalysts, *ACS Catal.* 6 (2016) 6892–6905.
- [18] C. Wang, D. Astruc, Recent developments of nanocatalyzed liquid-phase hydrogen generation, *Chem. Soc. Rev.* 50 (2021) 3437–3484.
- [19] Y.-Z. Chen, Q. Xu, S.-H. Yu, H.-L. Jiang, Tiny Pd@Co core-shell nanoparticles confined inside a metal-organic framework for highly efficient catalysis, *Small* 11 (2015) 71–76.
- [20] W. Chen, D. Li, Z. Wang, G. Qian, Z. Sui, X. Duan, X. Zhou, I. Yeboah, D. Chen, Reaction mechanism and kinetics for hydrolytic dehydrogenation of ammonia borane on a Pt/CNT catalyst, *AIChE J.* 63 (2017) 60–65.
- [21] J. Zhang, W. Chen, H. Ge, C. Chen, W. Yan, Z. Gao, J. Gan, B. Zhang, X. Duan, Y. Qin, Synergistic effects in atomic-layer-deposited PtCox/CNTs catalysts enhancing hydrolytic dehydrogenation of ammonia borane, *Appl. Catal. B Environ.* 235 (2018) 256–263.
- [22] Q. Sun, N. Wang, R. Bai, Y. Hui, T. Zhang, D.A. Do, P. Zhang, L. Song, S. Miao, J. Yu, Synergistic effect of ultrasmall metal clusters and zeolites promoting hydrogen generation, *Adv. Sci.* 6 (2019), 1802350.
- [23] J. Li, Q. Guan, H. Wu, W. Liu, Y. Lin, Z. Sun, X. Ye, X. Zheng, H. Pan, J. Zhu, S. Chen, W. Zhang, S. Wei, J. Lu, Highly active and stable metal single-atom catalysts achieved by strong electronic metal-support interactions, *J. Am. Chem. Soc.* 141 (2019) 14515–14519.
- [24] H. Liu, C.Y. Cao, P. Li, Y. Yu, W.G. Song, Core-shell structured nanospheres with mesoporous silica shell and Ni core as a stable catalyst for hydrolytic dehydrogenation of ammonia borane, *J. Energy Chem.* 23 (2014) 50–56.
- [25] C. Wang, J. Tuninetti, Z. Wang, C. Zhang, R. Ciganda, L. Salmon, S. Moya, J. Ruiz, D. Astruc, Hydrolysis of ammonia-borane over Ni/ZIF-8 nanocatalyst: high efficiency, mechanism, and controlled hydrogen release, *J. Am. Chem. Soc.* 139 (2017) 11610–11615.
- [26] Z. Li, T. He, L. Liu, W. Chen, M. Zhang, G. Wu, P. Chen, Covalent triazine framework supported non-noble metal nanoparticles with superior activity for catalytic hydrolysis of ammonia borane: from mechanistic study to catalyst design, *Chem. Sci.* 8 (2017) 781–788.
- [27] L. Zhou, J. Meng, P. Li, Z. Tao, L. Mai, J. Chen, Ultrasmall cobalt nanoparticles supported on nitrogen-doped porous carbon nanowires for hydrogen evolution from ammonia borane, *Mater. Horiz.* 4 (2017) 268–273.

[28] K. Guo, H. Li, Z. Yu, Size-dependent catalytic activity of monodispersed nickel nanoparticles for the hydrolytic dehydrogenation of ammonia borane, *ACS Appl. Mater. Interfaces* 10 (2018) 517–525.

[29] C. Cui, Y. Liu, S. Mehdi, H. Wen, B. Zhou, J. Li, B. Li, Enhancing effect of Fe-doping on the activity of nano Ni catalyst towards hydrogen evolution from NH_3BH_3 , *Appl. Catal. B Environ.* 265 (2020), 118612.

[30] C. Wang, L. Li, X. Yu, Z. Lu, X. Zhang, X. Wang, X. Yang, J. Zhao, Regulation of d-band electrons to enhance the activity of Co-based non-noble bimetal catalysts for hydrolysis of ammonia borane, *ACS Sustain. Chem. Eng.* 8 (2020) 8256–8266.

[31] Y. Chen, Z. Lai, X. Zhang, Z. Fan, Q. He, C. Tan, H. Zhang, Phase engineering of nanomaterials, *Nat. Rev. Chem.* 4 (2020) 243–256.

[32] H. Cheng, N. Yang, Q. Lu, Z. Zhang, H. Zhang, Syntheses and properties of metal nanomaterials with novel crystal phases, *Adv. Mater.* 30 (2018), 1707189.

[33] X. Tan, S. Geng, Y. Ji, Q. Shao, T. Zhu, P. Wang, Y. Li, X. Huang, Closest packing polymorphism interfaced metastable transition metal for efficient hydrogen evolution, *Adv. Mater.* 32 (2020), 2002857.

[34] J.-X. Liu, H.-Y. Su, D.-P. Sun, B.-Y. Zhang, W.-X. Li, Crystallographic dependence of CO activation on cobalt catalysts: HCP versus FCC, *J. Am. Chem. Soc.* 135 (2013) 16284–16287.

[35] Z.-P. Wu, S. Shan, Z.-H. Xie, N. Kang, K. Park, E. Hopkins, S. Yan, A. Sharma, J. Luo, J. Wang, V. Petkov, L. Wang, C.-J. Zhong, Revealing the role of phase structures of bimetallic nanocatalysts in the oxygen reduction reaction, *ACS Catal.* 8 (2018) 11302–11313.

[36] J. Liang, F. Ma, S. Hwang, X. Wang, J. Sokolowski, Q. Li, G. Wu, D. Su, Atomic arrangement engineering of metallic nanocrystals for energy-conversion electrocatalysis, *Joule* 3 (2019) 956–991.

[37] S. Zhu, X. Li, J. Kang, X. Duan, S. Wang, Persulfate activation on crystallographic manganese oxides: mechanism of singlet oxygen evolution for nonradical selective degradation of aqueous contaminants, *Environ. Sci. Technol.* 53 (2019) 307–315.

[38] H. Li, X. Zhou, W. Zhai, S. Lu, J. Liang, Z. He, H. Long, T. Xiong, H. Sun, Q. He, Z. Fan, H. Zhang, Phase engineering of nanomaterials for clean energy and catalytic applications, *Adv. Energy Mater.* 10 (2020), 2002019.

[39] Y. Zheng, Y. Jiao, Y. Zhu, L.H. Li, Y. Han, Y. Chen, M. Jaroniec, S.-Z. Qiao, High electrocatalytic hydrogen evolution activity of an anomalous ruthenium catalyst, *J. Am. Chem. Soc.* 138 (2016) 16174–16181.

[40] C. Wang, Y. Wang, H. Yang, Y. Zhang, H. Zhao, Q. Wang, Revealing the role of electrocatalyst crystal structure on oxygen evolution reaction with nickel as an example, *Small* 14 (2018), 1802895.

[41] J. Li, Z. Li, F. Zhan, M. Shao, Phase engineering of cobalt hydroxide toward cation intercalation, *Chem. Sci.* 12 (2021) 1756–1761.

[42] P. Chen, K. Xu, S. Tao, T. Zhou, Y. Tong, H. Ding, L. Zhang, W. Chu, C. Wu, Y. Xie, Phase-transformation engineering in cobalt diselenide realizing enhanced catalytic activity for hydrogen evolution in an alkaline medium, *Adv. Mater.* 28 (2016) 7527–7532.

[43] S. De, J. Zhang, R. Luque, N. Yan, Ni-based bimetallic heterogeneous catalysts for energy and environmental applications, *Energy Environ. Sci.* 9 (2016) 3314–3347.

[44] J. Gong, L.L. Wang, Y. Liu, J.H. Yang, Z.G. Zong, Structural and magnetic properties of hcp and fcc Ni nanoparticles, *J. Alloy. Compd.* 457 (2008) 6–9.

[45] M. Richard-Plouet, M. Guillot, S. Vilminot, C. Leuvrey, C. Estournès, M. Kurmoor, hcp and fcc nickel nanoparticles prepared from organically functionalized layered phyllosilicates of nickel(II), *Chem. Mater.* 19 (2007) 865–871.

[46] G. Zhao, J. Zhong, J. Wang, T.-K. Sham, X. Sun, S.-T. Lee, Revealing the synergistic effects in Ni nanoparticle–carbon nanotube hybrids by scanning transmission X-ray microscopy and their application in the hydrolysis of ammonia borane, *Nanoscale* 7 (2015) 9715–9722.

[47] Q. Yao, Z.-H. Lu, Y. Yang, Y. Chen, X. Chen, H.-L. Jiang, Facile synthesis of graphene-supported Ni-CeO_x nanocomposites as highly efficient catalysts for hydrolytic dehydrogenation of ammonia borane, *Nano Res.* 11 (2018) 4412–4422.

[48] H. Wang, Y. Zhao, F. Cheng, Z. Tao, J. Chen, Cobalt nanoparticles embedded in porous N-doped carbon as long-life catalysts for hydrolysis of ammonia borane, *Catal. Sci. Technol.* 6 (2016) 3443–3448.

[49] Y. Wu, X. Wu, Q. Liu, C. Huang, X. Qiu, Magnetically recyclable Ni@h-BN composites for efficient hydrolysis of ammonia borane, *Int. J. Hydrog. Energy* 42 (2017) 16003–16011.

[50] X. Yang, Q. Li, L. Li, J. Lin, X. Yang, C. Yu, Z. Liu, Y. Fang, Y. Huang, C. Tang, CuCo binary metal nanoparticles supported on boron nitride nanofibers as highly efficient catalysts for hydrogen generation from hydrolysis of ammonia borane, *J. Power Sources* 431 (2019) 135–143.

[51] M. Kuang, Q. Wang, P. Han, G. Zheng, Cu, Co-embedded N-enriched mesoporous carbon for efficient oxygen reduction and hydrogen evolution reactions, *Adv. Energy Mater.* 7 (2017), 1700193.

[52] F. Li, G.-F. Han, H.-J. Noh, S.-J. Kim, Y. Lu, H.Y. Jeong, Z. Fu, J.-B. Baek, Boosting oxygen reduction catalysis with abundant copper single atom active sites, *Energy Environ. Sci.* 11 (2018) 2263–2269.

[53] C. Wan, L. Sun, L. Xu, D.-G. Cheng, F. Chen, X. Zhan, Y. Yang, Novel NiPt alloy nanoparticle decorated 2D layered g-C₃N₄ nanosheets: a highly efficient catalyst for hydrogen generation from hydrous hydrazine, *J. Mater. Chem. A* 7 (2019) 8798–8804.

[54] P. Li, R. Chen, S. Tian, Y. Xiong, Efficient oxygen evolution catalysis triggered by nickel phosphide nanoparticles compositing with reduced graphene oxide with controlled architecture, *ACS Sustain. Chem. Eng.* 7 (2019) 9566–9573.

[55] P. Li, H.C. Zeng, Sandwich-like nanocomposite of CoNiO_x/reduced graphene oxide for enhanced electrocatalytic water oxidation, *Adv. Funct. Mater.* 27 (2017), 1606325.

[56] Z. Xin, Z. Yufei, J. Xiaodan, Z. Yunxuan, S. Lu, W. Qing, W.G. I. N, W. Li-Zhu, T. Chen-Ho, Z. Tierui, Silica-protected ultrathin Ni₃FeN Nanocatalyst for the efficient hydrolytic dehydrogenation of NH_3BH_3 , *Adv. Energy Mater.* 8 (2018), 1702780.

[57] Y. Lin, L. Yang, H. Jiang, Y. Zhang, D. Cao, C. Wu, G. Zhang, J. Jiang, L. Song, Boosted reactivity of ammonia borane dehydrogenation over Ni/Ni₂P heterostructure, *J. Phys. Chem. Lett.* 10 (2019) 1048–1054.